ADVANCED FUNCTIONAL MATERIALS

Supporting Information

for *Adv. Funct. Mater.*, DOI 10.1002/adfm.202404361

An Efficient Fiber Gel Dye-Sensitized Solar Cell with Stable Interlaced Interfaces

Xinyue Kang, Jiatian Song, Jiuzhou Liu, Siwei Cao, Zhengmeng Lin, Hongyu Jiang, Yiqing Yang, Xiangran Cheng, Yulu Ai, Xuemei Sun, Kaiwen Zeng, Zhengfeng Zhu and Huisheng Peng**

Supporting Information for

An Efficient Fiber Gel Dye-Sensitized Solar Cell with Stable Interlaced Interfaces

Xinyue Kang, Jiatian Song, Jiuzhou Liu, Siwei Cao, Zhengmeng Lin, Hongyu Jiang, Yiqing Yang, Xiangran Cheng, Yulu Ai, Xuemei Sun, Kaiwen Zeng, Zhengfeng Zhu and Huisheng Peng**

State Key Laboratory of Molecular Engineering of Polymers, Department of Macromolecular Science, and Institute of Fiber Materials and Devices, Fudan University, Shanghai 200438, China.

Corresponding Email: zhuzf@fudan.edu.cn; penghs@fudan.edu.cn.

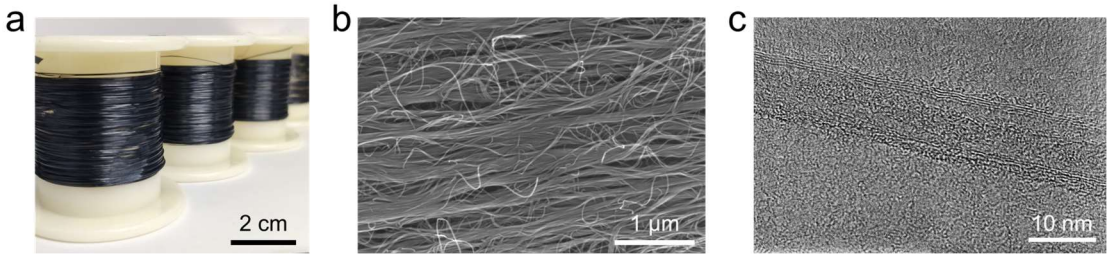

Figure S1. a) Photograph of CNT fibers winded on reels. b) SEM image of CNT fiber with aligned structure. (c) Transmission electron microscope image of a multi-walled CNT.

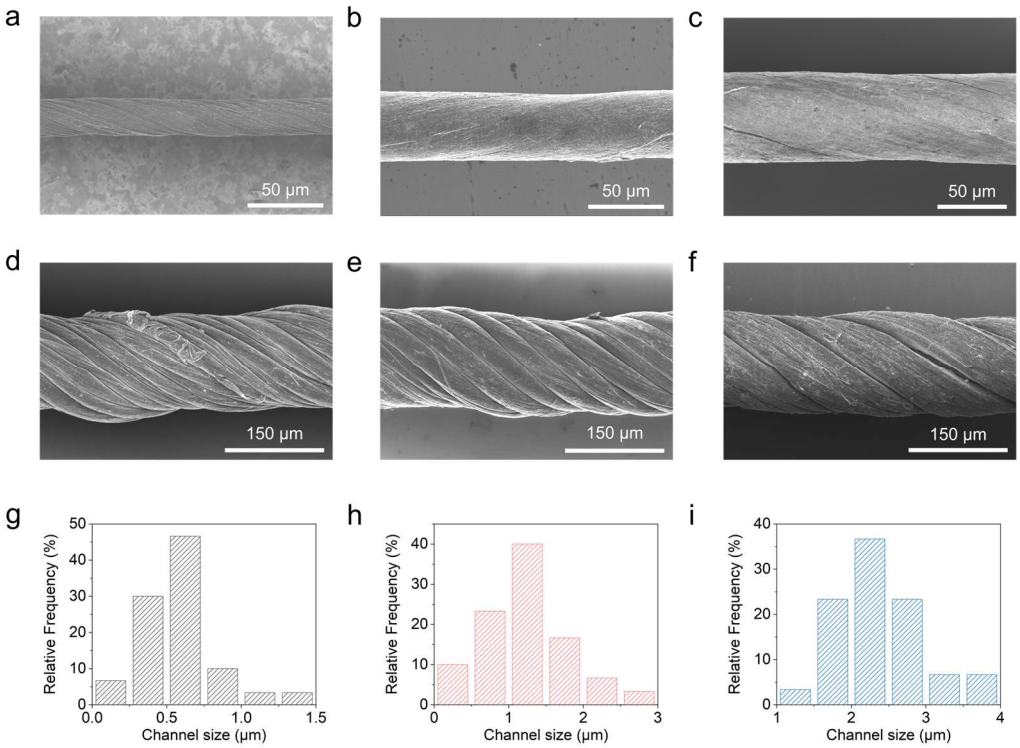

Figure S2. a–c) SEM images of the primary CNT fibers with diameters of 25, 45, and 65 μm, respectively. d–f) SEM images of the counter electrode with a diameter of ~150 μm prepared by twisting the primary CNT fibers with diameters of 25, 45, and 65 μm, respectively. g–i) Corresponding statistical distributions of the aligned channels in (d–f), 0.58±0.27 μm (g), 1.27±0.53 μm (h), and 2.34±0.62 μm (i). Each determined channel size was the average value of 50 channel sizes measured at different parts of a fiber counter electrode from SEM images.

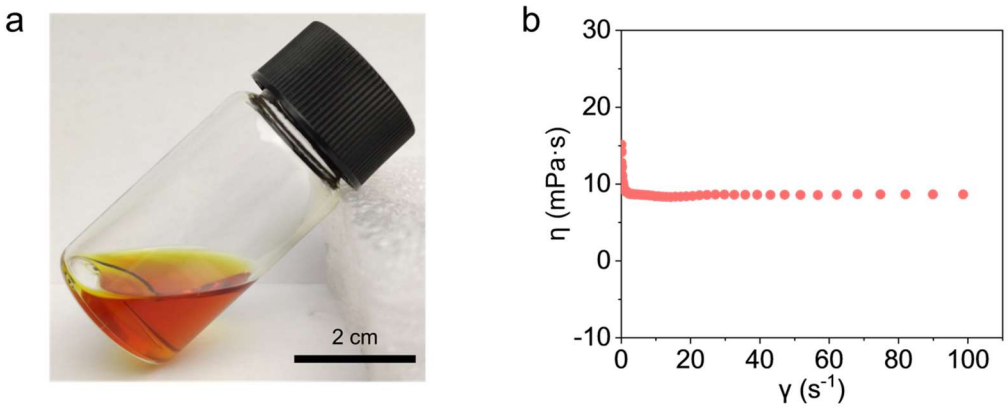

Figure S3. a) Photograph of the electrolyte precursor solution. b) Viscosity of the precursor solution with a liquid content of 86 wt% at 25 °C.

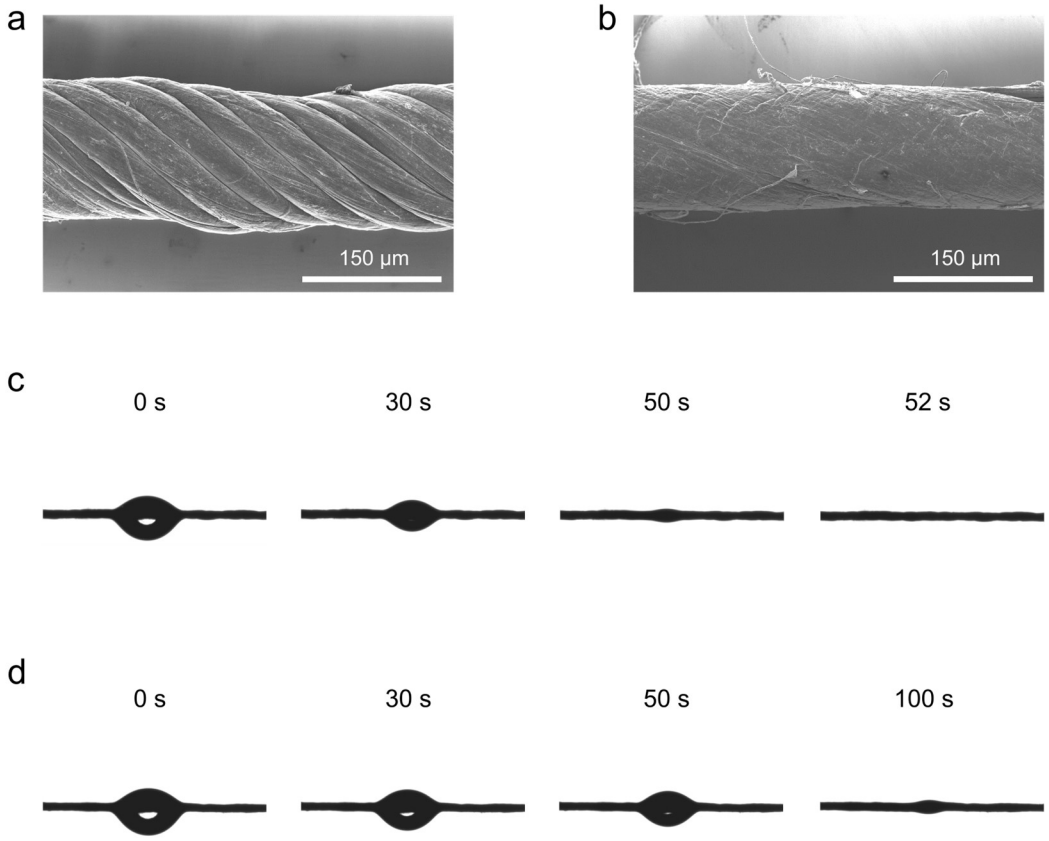

Figure S4. a, b) SEM images of the CNT fibers with and without aligned channels, respectively. c, d) Photographs of a droplet of precursor solution on the surface of fibers with and without aligned channels at different times, respectively.

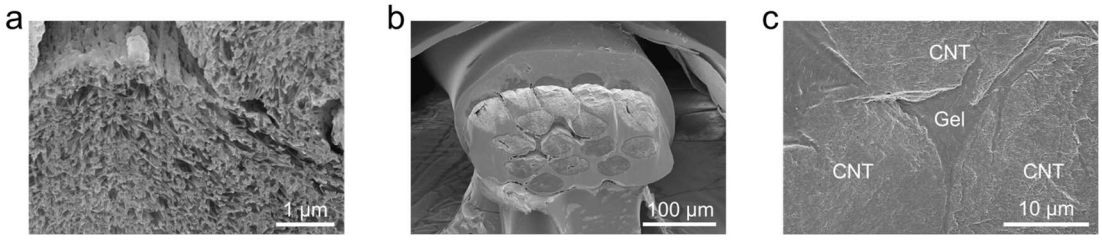

Figure S5. a) Cross-sectional SEM image of the initial CNT fiber. b, c) Cross-sectional SEM images of the CNT fiber embedded in the gel electrolyte at low and high resolutions, respectively.

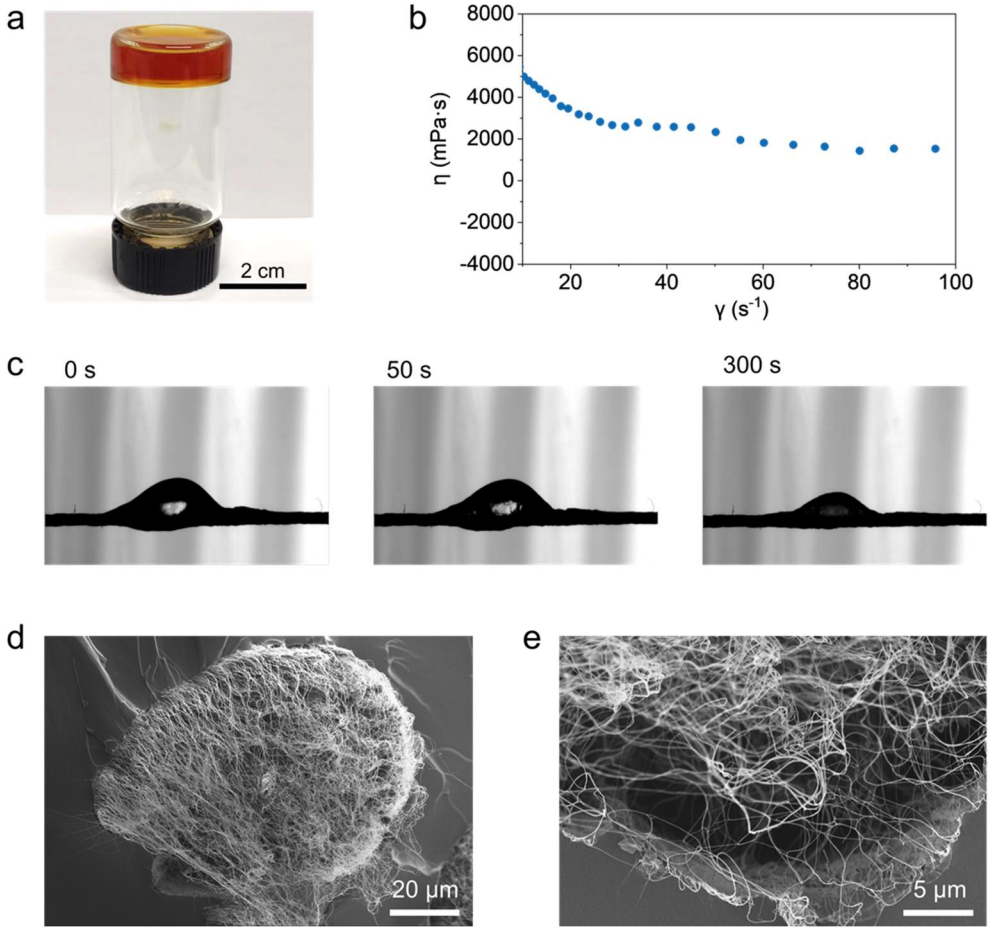

Figure S6. a) Photograph of P(VDF-HFP)-based gel electrolyte prepared by dissolving 14 wt% P(VDF-HFP) in methoxypropionitrile-based liquid electrolyte. The gel electrolyte cannot flow at room temperature. b) Viscosity of P(VDF-HFP)-based gel electrolyte at 80 ºC. c) Photographs of a preheated droplet of P(VDF-HFP)-based gel electrolyte on the surface of CNT fibers at different times. The droplet cannot fully infiltrate the CNT fiber before loss of fluidity. d, e) Cross-sectional SEM images of a CNT fiber embedded with P(VDF-HFP)-based gel electrolyte at low and high resolutions, respectively. The P(VDF-HFP)-based gel electrolyte can neither penetrate into the CNT fiber, nor adhere tightly to its surface.

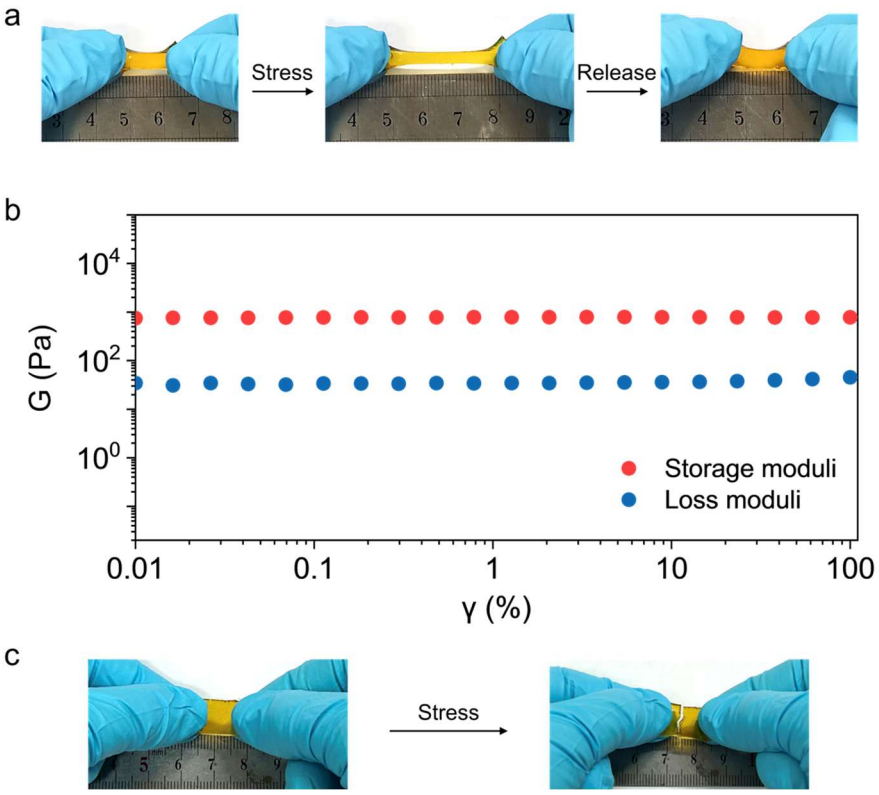

Figure S7. a) Photographs of PU-based gel electrolyte in pristine, stretched and released states, indicating good stretchability and resilience. b) Strain sweep curve of PU-based gel electrolyte at a frequency of 1 Hz. The storage moduli were higher than loss moduli representing its elastic state. c) Photographs of P(VDF-HFP)-based gel electrolyte in pristine and stretched states showing brittleness.

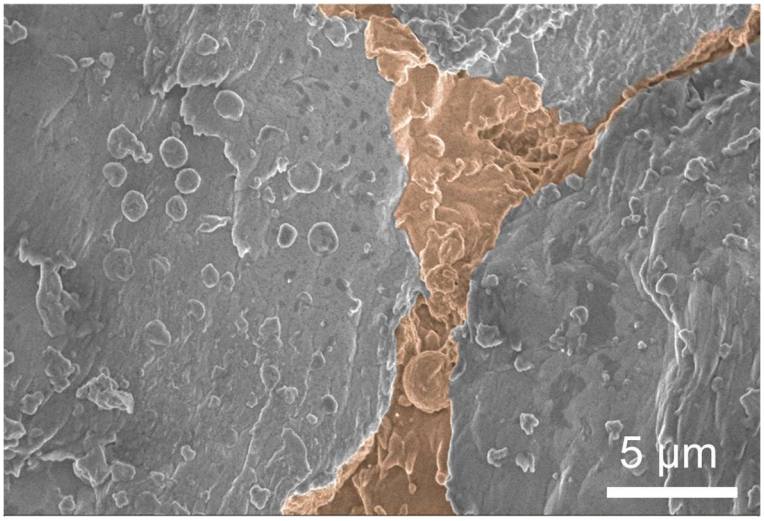

Figure S8. Cross-sectional SEM image of the interfaces between counter electrode and gel electrolyte with interlaced structure after bending for 5,000 cycles. To identify the fiber electrodes and gel electrolyte for convenience, an orange layer was added to the region of gel electrolyte.

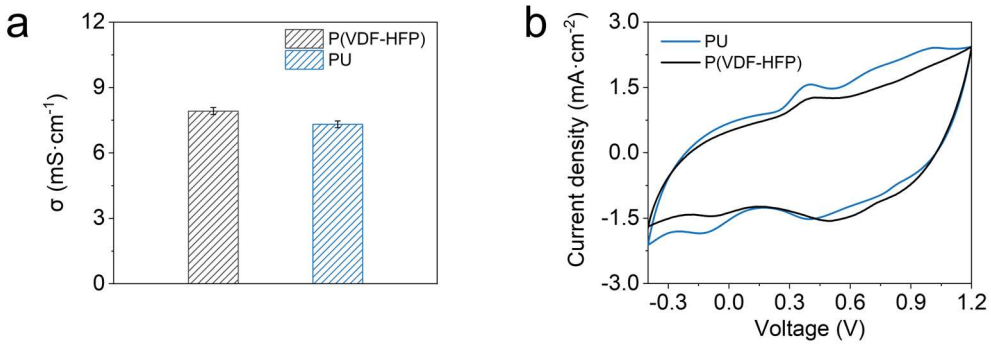

Figure S9. a) The conductivities of P(VDF-HFP)-based (7.92±0.16 mS·cm^{-1}) and PU-based (7.31±0.16 mS·cm^{-1}) gel electrolyte. They had equal liquid contents of 86 wt%. Error bars show standard deviations for the results from three samples. b) Cyclic voltammograms of the counter electrodes incorporated with P(VDF-HFP)-based and PU-based gel electrolyte, showing reduction peak current densities of −1.455 mA·cm^{-2} at −0.1 V and −1.847 mA·cm^{-2} at −0.144 V, and peak-to-peak voltage separations of 0.526 V and 0.549 V, respectively.

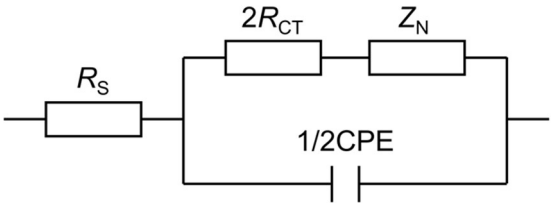

Figure S10. The equivalent circuit of the Nyquist plot. (R_S: series resistance; R_{CT}: charge transfer resistance; Z_N: Nernst diffusion impedances; CPE: constant phase angle element).

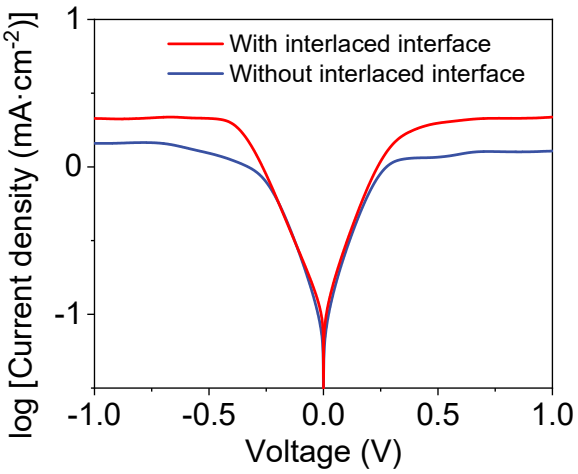

Figure S11. Tafel polarization curves of symmetrical dummy cells fabricated with two identical electrodes in the gel electrolyte, measured by linear sweep voltammetry at a scan rate of 10 $mV \cdot s^{-1}$. The exchange current densities of the counter electrode with and without interlaced interfaces were 0.90 and 0.49 $mA \cdot cm^{-2}$, respectively.

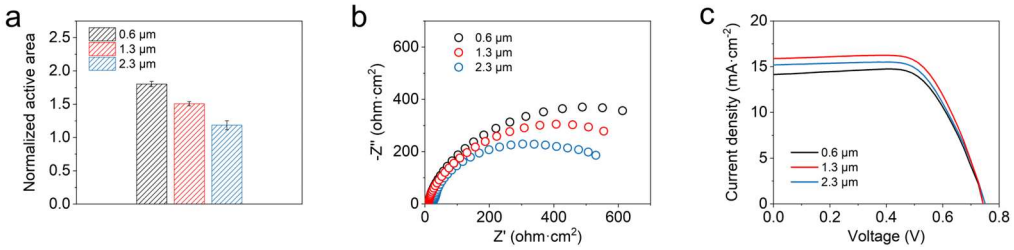

Figure S12. a) Normalized areas of the CNT fibers with channel sizes of 0.6, 1.3 and 2.3 μm were 1.80±0.04, 1.51±0.03 and 1.18±0.07, respectively. Error bars show standard deviations for the results from three samples. b) Nyquist plots of symmetrical cells with two identical electrodes measured at 0 V from 100 kHz to 0.01 Hz. Nernst diffusion impedances of the CNT fibers with channel sizes of 0.6, 1.3 and 2.3 μm were 945.2, 787.5 and 605.1 Ω·cm^2, respectively. c) *J-V* curves of FGDSCs consisting of CNT fibers with different channel sizes. The detailed parameters are shown at Table S1.

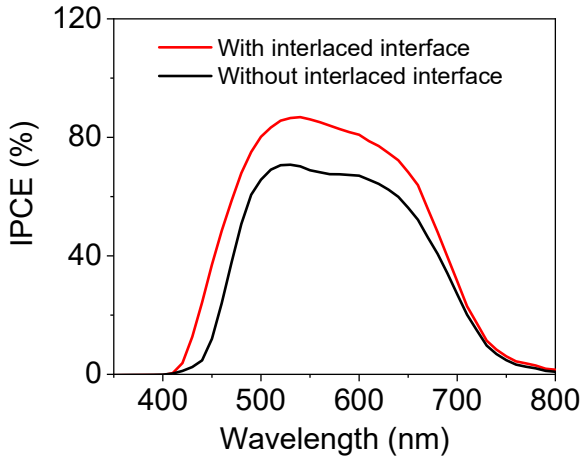

Figure S13. IPCE spectra of the FGDSCs with and without interlaced interfaces. The integrated current density of the FGDSC with interlaced interfaces was increased by 26.2%.

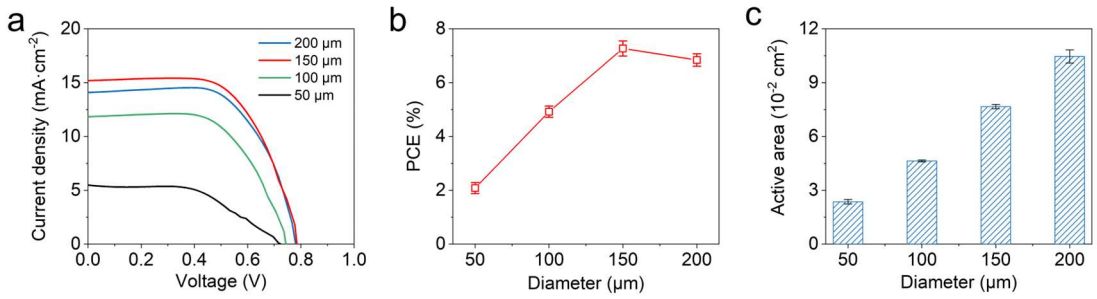

Figure S14. a) *J-V* curves of FGDSCs using CNT fiber counter electrodes with different diameters. b) PCEs of FGDSCs using CNT fiber counter electrodes with diameters of 50, 100, 150, and 200 μm were 2.08%, 4.92%, 7.27%, and 6.84%, respectively. Error bars show standard deviations for the results from three samples. c) Active areas of CNT fiber counter electrodes with diameters of 50, 100, 150, and 200 μm were (2.36±0.12) × 10^{-2}, (4.64±0.06) × 10^{-2}, (7.66±0.12) × 10^{-2}, and (10.46±0.37) × 10^{-2} cm^2, respectively. Error bars show standard deviations for the results from three samples.

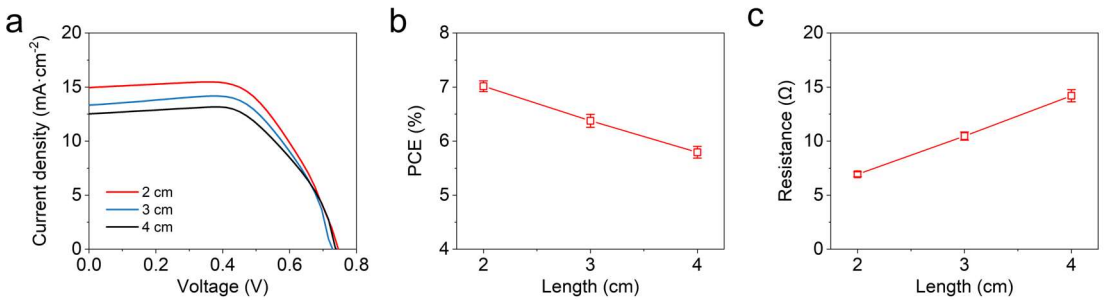

Figure S15. a) *J-V* curves of FGDSCs using CNT fiber counter electrodes with different lengths. b) PCEs of FGDSCs using CNT fiber counter electrodes with lengths of 2, 3, and 4 cm were 7.01%, 6.38%, and 5.79%, respectively. Error bars show standard deviations for the results from three samples. c) Resistances of CNT fiber counter electrodes with lengths of 2, 3, and 4 cm were 6.93±0.23, 10.47±0.38, and 14.20±0.56 Ω, respectively. Error bars show standard deviations for the results from three samples.

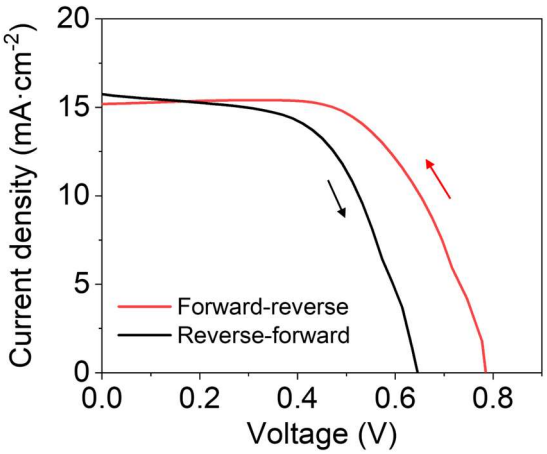

Figure S16. *J-V* curves of an FGDSC measured in forward and reverse directions. (Forward-reverse: from forward bias to reverse bias; Reverse-forward: from reverse bias to forward bias). The PCE, V_{OC}, J_{SC}, and FF of the FGDSC measured from forward bias to reverse bias were 7.51%, 0.79 V, 15.19 mA·cm^{-2}, and 0.63, respectively. The PCE, V_{OC}, J_{SC}, and FF of the FGDSC measured from reverse bias to forward bias were 5.97%, 0.65 V, 15.86 mA·cm^{-2}, and 0.58, respectively.

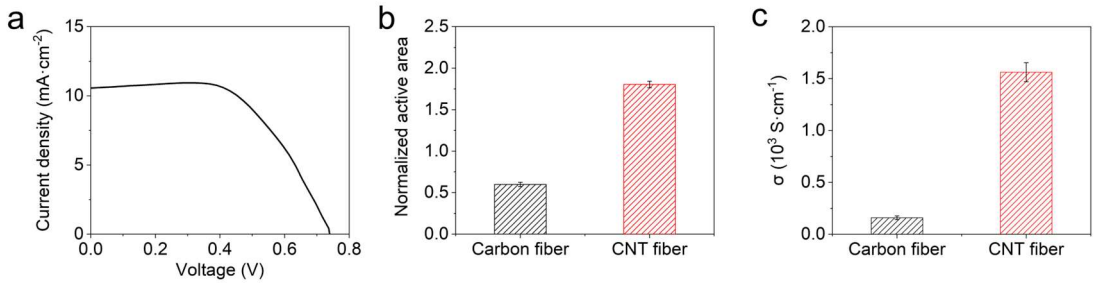

Figure S17. a) *J-V* curve of FGDSC using the carbon fiber-based counter electrode and PU-based gel electrolyte. The PCE, V_{OC}, J_{SC}, and FF of the FGDSC were 4.56%, 0.74 V, 10.57 mA·cm^{-2}, and 0.58, respectively. b) Normalized active areas of the carbon fiber and CNT fiber were 0.60±0.03 and 1.80±0.04, respectively. Error bars show standard deviations for the results from three samples. c) The conductivities of carbon fiber and CNT fiber were (0.16±0.02) × 10^3 and (1.56±0.09) × 10^3 S·cm^{-1}, respectively. Error bars show standard deviations for the results from three samples.

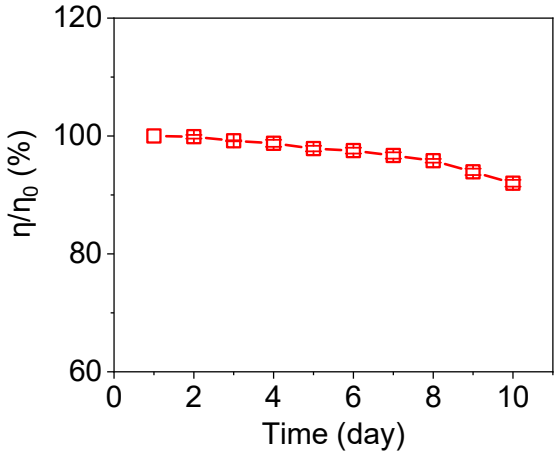

Figure S18. PCE variations of the FGDSCs placed at 25 ℃ and a humidity of 20% for 10 days. Error bars show standard deviations for the results from three samples.

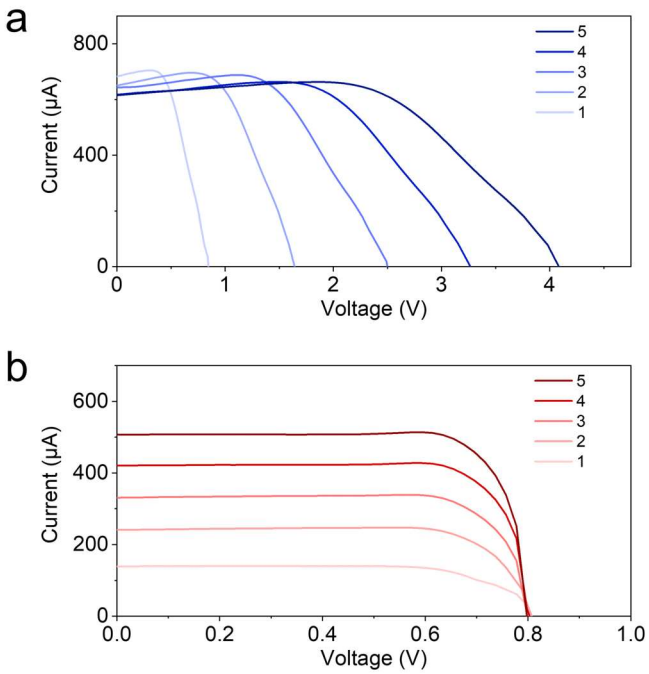

Figure S19. a, b) *I–V* curves of FGDSCs connected in series and in parallel, respectively.

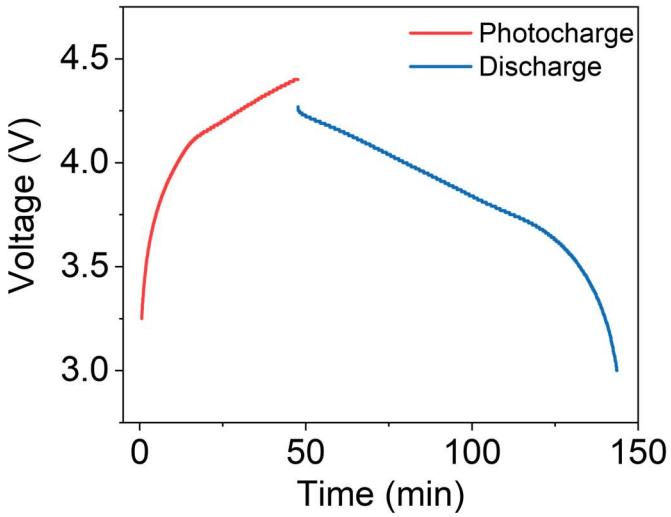

Figure S20. Photocharge/discharge curves of self-charging power system. A fiber lithium-ion battery was charged from 3.0 to 4.4 V by FDSSCs under simulated AM1.5G sunlight and then discharged to 3.0 V at 0.5 C rate.

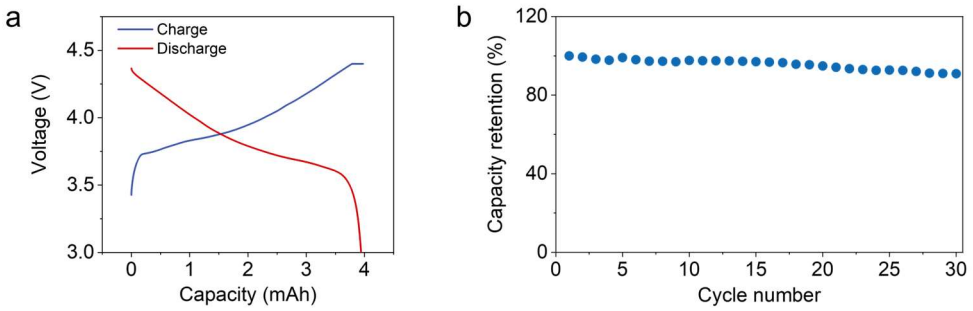

Figure S21. Typical charge and discharge profiles of a fiber lithium-ion battery. The fiber lithium-ion battery was charged from 3.0 to 4.4 V at 0.3C rate, and subsequently discharged to 3.0 V at 0.5C rate, showing a capacity of 3.9 mAh. b) Cycling stability of the fiber lithium-ion battery. The fiber lithium-ion battery was charged to 4.4 V at 0.3C rate, and then discharged to 3.0 V at 0.5C rate.

Table S1. Photovoltaic parameters of the FGDSCs in Figures S9c and 4a.

	V_{OC}/(V)	J_{SC}/(mA·cm^{-2})	FF	PCE/(%)
Without interlaced structure	0.73	12.61	0.62	5.73
With interlaced structure (0.6 μm)	0.75	14.15	0.68	7.15
With interlaced structure (1.3 μm)	**0.75**	**15.88**	**0.67**	**7.95**
With interlaced structure (2.3 μm)	0.76	15.20	0.65	7.51

Table S2. Structure and photovoltaic parameters of the FGDSCs in Figure 4b.

	Device structure	V_{OC} (V)	J_{SC} (mA·cm^{-2})	FF	PCE (%)	Ref.
Solid-state	PBT/Cu/Mn/ZnO/CuI/ Cu-plated polybutylene terephthalate	0.46	7.8	0.36	1.30	[1]
	Ti/TiO_2/N719/CuI/Ag-plated nylon yarns	0.4	9.42	0.51	1.92	[2]
	Ti/TiO_2/N719/lithium bis-(trifluoromethanesulfonyl)imide (Li-TFSI) electrolyte with 4-hydroxy-2,2,6,6-tetramethylpiperidin-1-oxyl (TEMPOL)	0.66	12.28	0.76	6.16	[3]
	Ti/TiO_2/N719/Li-TFSI/CNT yarn	0.67	8.32	0.72	4.00	[4]
	Ti/TiO_2/N719/polycarbonate-based electrolyte/Pt@MoO_3	0.66	10.21	0.76	5.11	[5]
	Ti/TiO_2/Ag@SiO_2 NPs/N719/Li-TFSI/Pt	0.68	10.37	0.76	5.38	[6]
	Ti/TiO_2/N719/polycarbonate-based electrolyte/Pt@MoO_3	0.74	11.05	0.75	6.41	[7]
	Ti/TiO_2/N719/Li-TFSI/CNT yarns dipped with $FeCl_3$	0.71	10.10	0.76	5.50	[8]
	Ti/TiO_2/N719/Li-TFSI/Pt	0.64	13.84	0.68	6.00	[9]
	Ti/TiO_2/N719/Li-TFSI with high stability electrolyte/Pt	0.71	12.20	0.74	6.50	[10]

Solid-state	Ti/TiO_2/N719/Pt-sputtered Li-TFSI/Pt	0.71	11.63	0.73	6.09	[11]
	Ti/TiO_2/Z907/Li-TFSI/ZIF-67/Pt	0.67	14.40	0.73	7.03	[12]
Quasi-solid-state	Ti/TiO_2/N719/1-ethyl-3-methylimidazolium iodide and 1-propyl-3-methylimidazolium iodide/multiwalled CNT	0.61	7.29	0.58	2.60	[13]
	Ti/TiO_2/N719/1-propyl-3-methylimidazolium iodide/CNT@Pt	0.61	9.51	0.61	3.51	[14]
	Ti/TiO_2/N719/1-butyl-3-methylimidazolium bis(trifluoromethanesulfonyl)imide and methoxypropionitrile solution of PVDF/CNT	0.7	15.32	0.51	5.47	[15]
	Ti/TiO_2/N719/PVDF-HFP/Pt	0.69	14.95	0.61	6.32	[16]
	Ti/TiO_2/N719/ in-situ polymerized PU-based electrolyte /CNT fibers with aligned channels	0.75	15.88	0.67	7.95	This work

References

[1] N. Zhang, J. Chen, Y. Huang, W. Guo, J. Yang, J. Du, X. Fan, C. Tao, *Adv. Mater.* **2015**, *28*, 263.

[2] Z. Gao, P. Liu, X. Fu, L. Xu, Y. Zuo, B. Zhang, X. Sun, H. Peng, *J. Mater. Chem. A* **2019**, *7*, 14447.

[3] J. H. Kim, S.-J. Koo, H. Cho, J. W. Choi, S. Y. Ryu, J.-W. Kang, S.-H. Jin, C. Ahn, M. Song, *ACS Sustain. Chem. Eng.* **2020**, *8*, 15065.

[4] J. H. Kim, S. K. Hong, S.-J. Yoo, C. Y. Woo, J. W. Choi, D. Lee, J.-W. Kang, H. W. Lee, M. Song, *Dyes Pigm.* **2021**, *185*, 108855.

[5] D. S. Utomo, J. H. Kim, D. Lee, J. Park, Y.-C. Kang, Y. H. Kim, J. W. Choi, M. Song, *J. Colloid Interface Sci.* **2021**, *584*, 520.

[6] J. H. Kim, S.-J. Yoo, D. Lee, J. W. Choi, S.-C. Han, T. I. Ryu, H. W. Lee, M. Shin, M. Song, *Nano Res.* **2021**, *14*, 2728.

[7] J. H. Kim, D. S. Utomo, D. Lee, J. W. Choi, M. Song, *J. Power Sources* **2021**, *512*, 230496.

[8] J. H. Kim, S.-J. Koo, J. Y. Cheon, Y. Jung, S. Cho, D. Lee, J. W. Choi, T. Kim, M. Song, *Nano Energy* **2022**, *96*, 107054.

[9] P. An, J. H. Kim, M. Shin, S. Kim, S. Cho, C. Park, G. Kim, H. W. Lee, J. W. Choi, C. Ahn, M. Song, *Nanomaterials* **2022**, *12*, 2309.

[10] J. Ho Kim, H. Woo Park, S.-J. Koo, D. Lee, E. Cho, Y.-K. Kim, M. Shin, J. Woo Choi, H. Jung Lee, M. Song, *J. Energy Chem.* **2022**, *67*, 458.

[11] J. H. Kim, D. S. Utomo, D. Lee, S. Cho, M. Song, J. W. Choi, *J. Mater. Chem. C* **2023**, *11*, 11980.

[12] J. H. Kim, E. Cho, G.-g. Kim, C. Park, S. Kim, S. Y. Ryu, J. W. Choi, H. J. Lee, M. Song, *Dyes Pigm.* **2023**, *219*, 111575.

[13] H. Sun, H. Li, X. You, Z. Yang, J. Deng, L. Qiu, H. Peng, *J. Mater. Chem. A* **2014**, *2*, 345.

[14] H. Li, Z. Yang, L. Qiu, X. Fang, H. Sun, P. Chen, S. Pan, H. Peng, *J. Mater. Chem. A* **2014**, *2*, 3841.

[15] H. Li, J. Guo, H. Sun, X. Fang, D. Wang, H. Peng, *ChemNanoMat* **2015**, *1*, 399.

[16] B.-C. Xiao, L.-Y. Lin, *J. Colloid Interface Sci.* **2020**, *571*, 126.